MATERIALS SCIENCE

Hot mixing: Mechanistic insights into the durability of ancient Roman concrete

Linda M. Seymour[1], Janille Maragh[1], Paolo Sabatini[2], Michel Di Tommaso[3], James C. Weaver[4], Admir Masic[1]*

Ancient Roman concretes have survived millennia, but mechanistic insights into their durability remain an enigma. Here, we use a multiscale correlative elemental and chemical mapping approach to investigating relict lime clasts, a ubiquitous and conspicuous mineral component associated with ancient Roman mortars. Together, these analyses provide new insights into mortar preparation methodologies and provide evidence that the Romans employed hot mixing, using quicklime in conjunction with, or instead of, slaked lime, to create an environment where high surface area aggregate-scale lime clasts are retained within the mortar matrix. Inspired by these findings, we propose that these macroscopic inclusions might serve as critical sources of reactive calcium for long-term pore and crack-filling or post-pozzolanic reactivity within the cementitious constructs. The subsequent development and testing of modern lime clast–containing cementitious mixtures demonstrate their self-healing potential, thus paving the way for the development of more durable, resilient, and sustainable concrete formulations.

INTRODUCTION

Ordinary Portland cement (OPC) is a key component of concrete, the most ubiquitous construction material in the world, but its production has serious environmental consequences. The manufacture of OPC releases up to 1 metric ton of CO_{2e} emissions per metric ton of produced material, and current strategies to reduce this impact are insufficient as demand continues to rise (*1*). These emissions are primarily generated when limestone and clay are calcined to form clinker (mainly tricalcium and dicalcium silicates, also known as alite and belite, respectively), which is then finely ground. One method to reduce cement's carbon footprint (which accounts for up to 8% of total global greenhouse gas emissions), is to improve the longevity of concrete through the incorporation of self-healing functionalities. The resulting extended use life, combined with a reduction in the need for extensive repair, could thus reduce the environmental impact and improve the economic life cycle of modern cementitious constructs (*2*).

In contrast to their modern counterparts, ancient Roman mortars and concretes have remained durable in a variety of climates, seismic zones, and even in direct contact with seawater, as in the case for maritime concrete. Because of this proven longevity on the order of millennia, these ancient construction materials are attractive model systems for the design of sustainable, durable cementitious composites for modern engineering applications (*3*–*5*).

For many centuries, and throughout the entire ancient Roman Empire, architectural elements, such as walls and foundations, and infrastructure systems, including aqueducts, roads, and bridges, were created from unreinforced concrete. This concrete was typically composed of volcanic tuff and other coarse aggregates (caementa), and bound by a mortar based on lime and pozzolanic materials such as volcanic ash (pulvis) (*6*), the detailed formulations of which were tailored to their specific intended applications (*7*, *8*). Whereas aerial lime mortars relied on the uptake of CO_2 from the air to harden, hydraulic mortars combined lime and water with reactive silicates and aluminosilicates (pozzolanic materials) to form cementitious hydrates [e.g., calcium alumino-silicate hydrates (C-A-S-H)] (*9*–*13*).

This reaction, also known as the pozzolanic reaction, can be written as

$$x\mathrm{Ca(OH)_2} + y\mathrm{Al_2O_3}\cdot z\mathrm{SiO_2} + (n-x)\mathrm{H_2O} \rightarrow (\mathrm{CaO})_x\cdot(\mathrm{SiO_2})_z\cdot(\mathrm{Al_2O_3})_y\cdot(\mathrm{H_2O})_{n-x}(\text{or C-A-S-H gel})$$

Any excess unreacted lime slowly carbonates in air via the reaction

$$\mathrm{Ca(OH)_2} + \mathrm{CO_2} \rightarrow \mathrm{CaCO_3} + \mathrm{H_2O}$$

By developing these hydraulic mortars, the Romans were able to create a stronger, more durable material that allowed them to build larger, more complex-shaped architectural structures for purposes that were not previously possible, including constructions in the sea (*14*–*16*).

The production process for Roman mortar began with the calcining of lime from a source such as limestone, marble, or travertine (all predominantly calcite, $CaCO_3$) to form quicklime [calcium oxide (CaO)] (*17*). This lime-based material, which can be hydrated using water (a process known as slaking) or added directly (a process known as hot mixing) (*18*–*21*), was then mixed with volcanic ash, ceramic fragments (cocciopesto), or other pozzolana, sand, and water to form the hydraulic mortar.

Regardless of the application, strict specifications for the raw materials were detailed by the ancient scholars Vitruvius and Pliny, especially for the limestone, which was to be pure white, so as to lack impurities (*6*, *17*). Previous studies on Roman architectural mortars determined that the calcined lime in these samples frequently contained <5 weight % oxides other than CaO (*7*, *14*). In recent years,

[1]Department of Civil and Environmental Engineering, Massachusetts Institute of Technology, Cambridge, MA 02139, USA. [2]DMAT srl, Udine, 33100, Italy. [3]IMM, Istituto Meccanica dei Materiali SA, via al Molino 55, 6916 Grancia, Switzerland. [4]Wyss Institute for Biologically Inspired Engineering, Harvard University, Cambridge, MA 02138, USA.
*Corresponding author. Email: masic@mit.edu

detailed investigations of ancient mortars and concretes allowed for the identification of some of the key chemical and mineralogical processes associated with interactions between pozzolanic materials and hydrated lime and provided insights into the mechanical performance of these materials (*11*, *12*, *22*–*26*).

Studies focusing on the durability of Roman concrete constructed in marine environments, for example, evidenced the dissolution of lime and vitric tuff clasts at high pH, followed by the precipitation of C-A-S-H–containing reaction rims and, subsequently, the post-setting crystallization of Al-tobermorite and phillipsite in the matrix (*11*, *27*). In both Augustan and Imperial era architectural concretes, a similar C-A-S-H precipitation and subsequent crystallization and growth of platy strätlingite crystals in the perimeters of scoriae and the cementing matrix were observed (*24*, *28*). More recently, both Al-tobermorite and strätlingite crystals were found in the mortars of the Augustan period (ca. 30 BCE) tomb of Caecilia Metella (*29*). The prolonged reactivity of volcanic aggregates and their potential role in the long-term durability of these materials has thus been an ongoing focus of recent studies on Roman concretes.

In addition to the features described above, aggregate-scale relict lime clasts, also referred to as remnant lime or lime lumps, are a ubiquitous and conspicuous feature of both architectural and maritime Roman concretes. The presence of these distinctive bright white features has been previously attributed to several scenarios including incomplete or over-burning during the calcining of lime (*20*), carbonation before concrete preparation (*30*), incomplete dissolution during setting (*12*), or insufficient mixing of the mortar (*14*).

In maritime structures, these lime clasts can be heterogeneous in composition; may contain calcite, vaterite, brucite, ettringite, hydrocalumite, C-A-S-H, tobermorite, and Al-tobermorite (*5*, *12*, *27*, *30*–*34*); and can be categorized into one of the following three groups: (i) geologic, (ii) partially dissolved, and (iii) fully dissolved (transformed) (*12*). Geologic inclusions are calcite-bearing aggregates that did not fully calcine during the production of quicklime. The other two, partially and fully dissolved clasts, have provided insight into the chemical evolution of maritime concretes. For example, partially dissolved clasts show a C-A-S-H–containing reaction rim, gradating toward a calcite-rich core (*12*). Fully dissolved clasts, in contrast, exhibit C-A-S-H throughout and, in some cases, the formation of Al-tobermorite (*12*, *27*). In both partially and fully dissolved clasts, the clast exteriors contain hydrocalumite and ettringite, attributed to hydration with seawater (*12*). Although these clasts are well characterized in maritime Roman concretes, less is known regarding the microstructure and chemical composition of relict lime clasts in open-air Roman constructions (structures on land) and the role that they might play in processes associated with the durability of these structures (*5*, *35*).

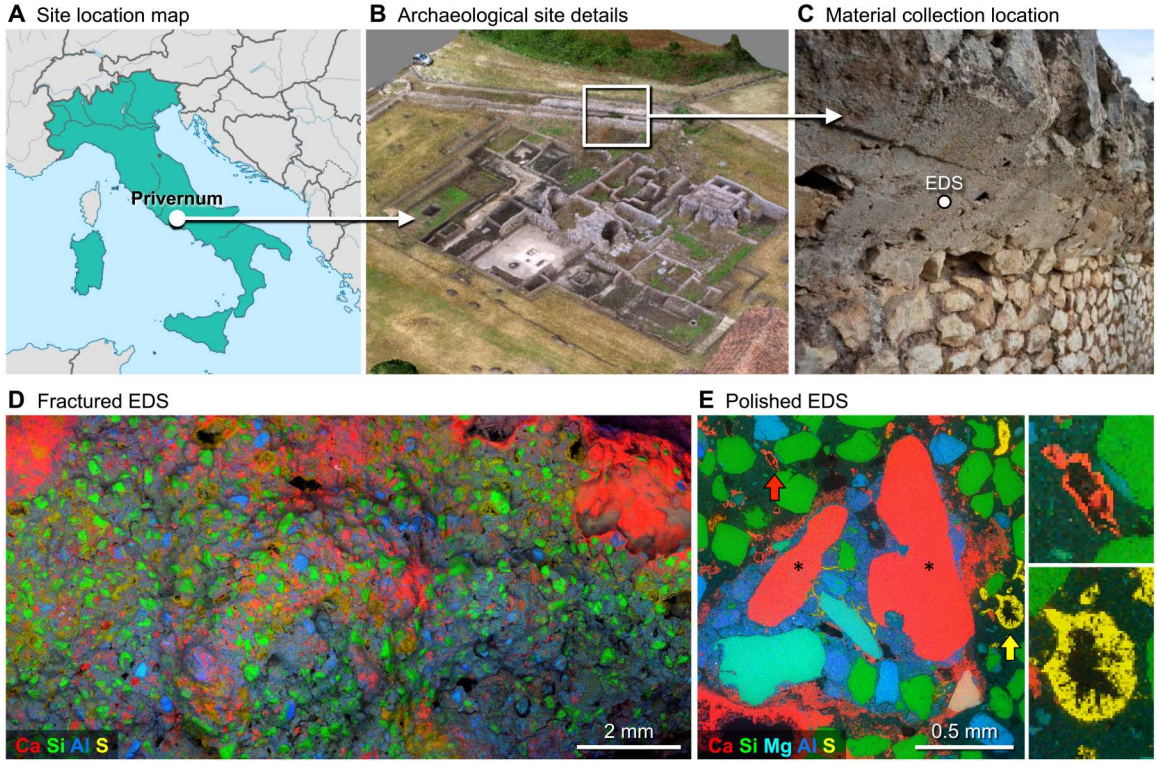

Fig. 1. Collection location and distinctive features of the ancient Roman concrete samples used in this study. The test samples came from the archaeological site of Privernum, near Rome, Italy (**A**), and shown as a photogrammetry-based three-dimensional reconstruction (**B**). The architectural mortar samples were collected from the bordering concrete city wall (**C**). Large-area EDS mapping of a fracture surface (**D**) reveals the calcium-rich (red), aluminum-rich (blue), silicon-rich (green), and sulfur-rich (yellow) regions of the mortar. Further imaging of polished cross-sections (**E**) shows aggregate-scale relict lime clasts within the mortar (the large red features denoted by asterisks). The colored arrows in (E) denote the pore-bordering rings visible in the EDS data that are rich in calcium (red) or sulfur (yellow), which are enlarged at right to show additional detail. Photo credits (B and C): Roberto Scalesse and Gianfranco Quaranta, Associazione AREA3, Italy.

To address these yet unresolved questions, we report on the chemical characterization of relict lime clasts found in 2000-year-old Roman concrete samples obtained from the archaeological site of Privernum, Italy. The investigated samples are compositionally consistent with other architectural mortars encountered throughout the Roman Empire (*8*, *13*, *16*, *36*, *37*), and were sourced from the masonry mortar of the city wall, an open-air structure. We characterized the composition of the lime clasts and their surrounding matrix using large-area scanning electron microscopy and energy dispersive x-ray spectroscopy (SEM-EDS), powder x-ray diffraction (XRD), and confocal Raman imaging. The results of these analyses provide compelling evidence for hot mixing of Roman mortar using quicklime instead of, or in addition to, slaked lime. From these findings, we propose that persistent, aggregate-scale, high surface area lime clasts that result from this process could serve as a source of reactive calcium for long-term pore and crack filling and therefore provide a chemically dominated intrinsic self-healing mechanism. Motivated by these discoveries, we developed a modern Roman-inspired cementitious mixture that incorporated a hot mixing preparation method and observed the effective self-healing of induced cracks measuring up to 0.5 mm in width. The results from our multiscale compositional analysis of Roman concrete and the development of their modern counterparts provide a starting point to understand the role of various production parameters on the durability of ancient mortars and concretes and demonstrate the applicability and potential value of these ancient design principles in the development of cementitious materials for the modern world.

RESULTS

The Roman mortar samples investigated in this work came from the ancient city of Privernum, near Rome, Italy (Fig. 1A). Privernum was occupied as early as the 2nd century BCE through the 13th century CE, and the site was first excavated in the 18th century, with the most recent work performed from 1990 to present. The samples analyzed in the present study were part of the city wall (Fig. 1, B and C), are compositionally consistent with other Roman concrete samples dating from the same time period (*8*), and correspond with the city's Roman occupation, which lasted through the fall of the empire.

To investigate centimeter-, millimeter-, and submillimeter-scale compositional details of the mortar samples, we used SEM-EDS. Large-area elemental mapping of the freshly fractured surface of a representative Roman mortar sample (Fig. 1D) shows its complex chemical composition (with a dominant presence of calcium, silicon, and aluminum), the aggregate-scale relict lime clasts, and evidence for pore filling by secondary mineral phases (fig. S1). Further elemental mapping of polished mortar samples (Fig. 1E) provided additional fine-scale structural and compositional information, the results of which were consistent with previous studies of Roman mortars and concretes (*11*, *12*, *27*). Note that to obtain reliable elemental mapping data from the irregularly fractured concrete samples, we used a multidetector EDS system, which both minimized the potential contributions of shadowing artifacts and facilitated the high-throughput analysis of a large number of test samples. In total, more than 15 different fractured and polished mortar sample regions were analyzed (from 10 different collected fragments) using this approach, and the results are representative of the trends observed.

These elemental maps (Fig. 1, D and E, and fig. S1) also show sulfur throughout the mortar, which, as proposed previously (*38*), could be due to primary sulfur originating from the components used to prepare the mortar, secondary sulfur that entered the binding matrix through the pores of the mortar, seen as rings, or a combination of these. While all of these considerations are possible, detailed elemental analysis (fig. S1) shows that sulfur is present primarily in the pore volume, with secondary sulfur likely originating from one or more of a variety of external, environmental sources including soil and acid rain. The latter intrusion is a common degradation pathway in which cementitious materials are leached on exposure to acid rain containing sulfur-based ions, as calcium carbonate is converted to calcium sulfate hydrates (e.g., gypsum) (*39*, *40*). Raman mapping (fig. S2) demonstrates that the sulfur-bearing pore walls contain predominantly gypsum, thus precluding the use of calcium sulfoaluminate fibers as a filling agent in these samples (*38*). Despite centuries of exposure to environmental attack, however, the masonry wall remains well preserved around the perimeter of the archaeological site.

To identify both the major and minor mineral phases present in the concrete wall samples and map their specific distribution patterns, we used two modes for quantitative analysis of the mortar's elemental composition: first on freshly fractured surfaces (Fig. 2, A to C) and second on prepared, polished cross-sections (Fig. 2, D to F). Quantitative EDS data were plotted pixel by pixel on ternary diagrams (Fig. 2, B and E) to reveal the relative ratios of the three key elements of the cementitious phases—calcium, silicon, and aluminum (*41*).

Immediately evident from these analyses is the compositional shift toward the (red) calcium vertex of the ternary diagram for the fractured surface (Fig. 2, A and B), suggesting that the sample likely failed along weaker binding phases, the relict lime clast, and the binder immediately surrounding the clast. Quantitative EDS data were then clustered to visualize the distribution of small differences in composition throughout the mortars. Points on the ternary diagrams (Fig. 2, B and E) and individual pixels on the original map area (Fig. 2, C and F) were colored on the basis of the assigned cluster. Within the polished cross-sections (Fig. 2F), the different investigated relict lime clasts all separated into two clusters—one within the clast reaction rim and another in the core. Evident here is a transition from the calcium-rich core to a rim containing higher concentrations of silicon and aluminum. Further analysis of the EDS maps also shows that the matrix immediately surrounding the lime clasts is richer in calcium than other parts of the matrix, suggesting that some leeching has occurred in the sample. Just outside the lime clasts and extending to the edge of the sample, a matrix phase rich in calcium with aluminum and silicon can also be seen. As shown in Fig. 2F, these points (red) are distinct from the primary binding phase (yellow), which has ratios of silicon, aluminum, and calcium more closely associated with C-A-S-H binders (*41*). Petrographic analysis (fig. S3) shows that the binder is predominantly isotropic, as would be the expected product from the pozzolanic reaction (poorly crystalline C-A-S-H), with calcite occurring in the matrix near lime clasts and within some pores.

A better understanding of the mineral assemblage and the potential identification of crystalline phases within the mortars was obtained through powder XRD. Two sample types were examined

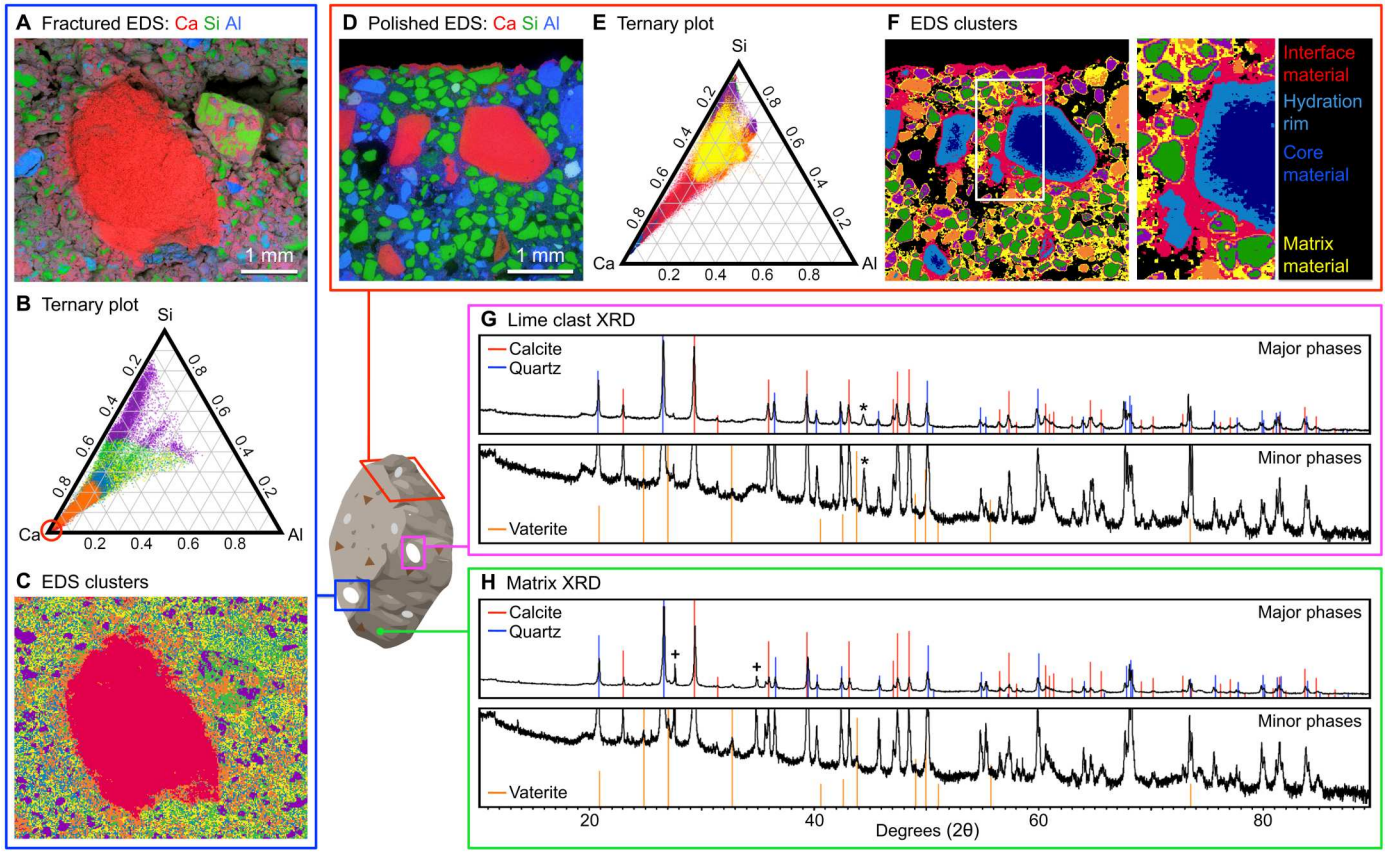

Fig. 2. Multimodal compositional analysis of ancient Roman concrete. EDS maps of a freshly fractured surface (**A**) and polished cross-section (**D**) are quantified, and each pixel is replotted as a relative ratio of calcium, silicon, and aluminum on a ternary diagram (**B** and **E**), with the most Ca-rich phases shown in red and denoted by the red circle near the Ca vertex in (B). Pixels in the ternary diagrams (B and E) and phase maps (**C** and **F**) were colored on the basis of the cluster of EDS data to which they belong. Surrounding each of the lime clasts is a clear rim of a compositionally unique phase (the hydration rim), which is denoted by the light blue zones in (F) and is shown at higher magnification at right with color-coded text for additional clarity. Powder XRD of a relict lime clast (**G**) and its surrounding matrix (**H**) confirms the presence of calcite and quartz and suggests the presence of vaterite among other phases [e.g., halite (*) and volcanic minerals (diopside, leucite, etc.) (+)] in the mortar.

in this way: extracted relict lime clasts from the mortars (Fig. 2G) and the binding matrix complete with other aggregate material (Fig. 2H). The remnant lime clasts were predominantly calcite and quartz (likely due to imperfect separation of the clast from surrounding binder and aggregates), although the diffraction data also suggest the presence of small quantities of potential recrystallization phases such as vaterite. Overall, the elemental and mineral assemblage in the Privernum mortar was well aligned with the composition of previously studied Roman mortar samples (*9*, *19*, *25*, *34*, *35*), highlighting the consistency of these samples from archaeological site to site.

Large-area SEM-EDS mapping of a representative resin-embedded cross-section of the Privernum mortar is shown in Fig. 3A. The relict lime clasts, identified by their high concentrations of Ca, were studied in detail using correlative EDS and Raman microspectroscopy (Fig. 3, B to E). The elemental composition of the lime clasts was clustered as described above to identify the distribution of compositional differences within the samples. The clustering results were plotted on the ternary axes (Fig. 3C) to characterize the relative ratios of the primary cementitious components. Six clusters were visualized corresponding to quartz aggregates, resin-rich regions, the cementitious matrix, two clusters within the lime clast, and one within the clast reaction rim. The reaction rim cluster is also seen incorporated into the cementitious matrix and corresponds to a composition range akin to calcium-enriched C-A-S-H phases (*41*). Each pixel of the lime clast region was recolored on the basis of the cluster that it belongs to in Fig. 3E.

High-resolution mapping data of the mineral phases in this same cross-section were obtained using Raman microspectroscopy (Fig. 3D). This methodology was chosen because the different calcium carbonate polymorphs of calcite, aragonite, and vaterite exhibit different Raman spectra due to the different binding environments within the crystal structures (*42*). Two carbonate-dominated phases were identified with this method. Specifically, one such phase (Fig. 3D, yellow) is characterized by a shift of −3 cm^{-1} of the ν_1 carbonate peak with respect to the 1085 cm^{-1} peak of calcite and a fluorescence signature distinct from the rest of the sample (fig. S4). The distribution of the phases identified through Raman spectroscopy is shown in Fig. 3E, and fig. S4 further demonstrates sample heterogeneity. In some of the relict lime clast spectra, a shoulder that can be associated with disordered $CaCO_3$ was present on the ν_1 peak (see fig. S5). Broadening of the ν_1 peak compared to a geologic Iceland spar calcite standard was also observed (fig. S6).

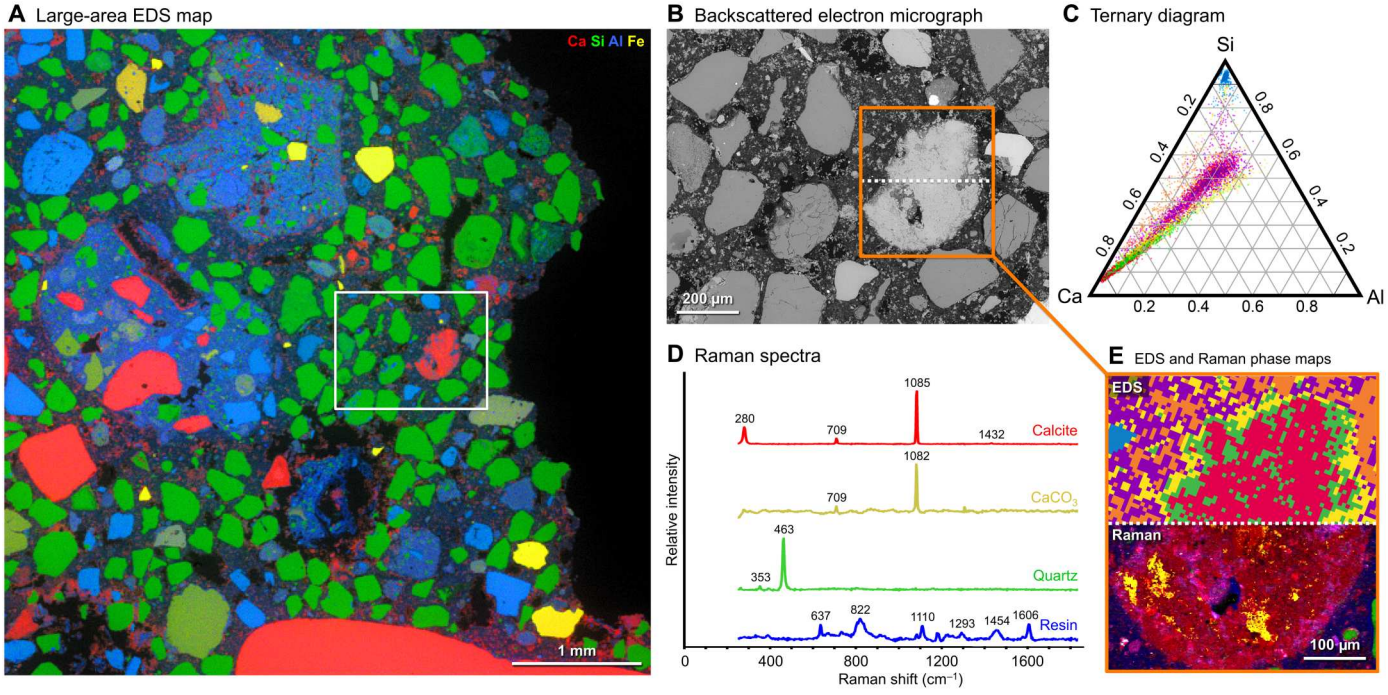

Fig. 3. Detailed analysis of lime clast elemental (EDS) and mineral (Raman) data. Large-area (5 mm image width) SEM-EDS elemental map of a polished Privernum wall section (**A**). The chemical composition of a representative lime clast (denoted with an orange box) is explored in detail (**B**). Elemental composition from quantified EDS shows six clusters, presented on a ternary diagram of calcium, silicon, and aluminum (**C**), which are colored on the basis of the cluster of EDS data to which they belong. Raman spectroscopy (**D**) reveals calcite (red), additional calcium carbonate phases (yellow), quartz (green), and resin (blue), with the characteristic peaks indicated. The distribution maps of the identified phases (**E**) are shown on the basis of their corresponding EDS and Raman scan data: quartz aggregates (blue), resin-rich regions (orange), the cementitious matrix (purple), two clusters within the lime clast (green and red), and a clast reaction rim (yellow).

The recent discovery of calcite-filled cracks in Roman concrete (*29*) suggested a potential long-term healing process that requires a Ca-rich source. Considering the ubiquity of relict lime clasts in Roman concrete (*5*, *12*, *24*, *43*) and their high surface area due to their particulate microstructure (Fig. 4, A to D), these inclusions might provide the requisite Ca reservoirs for these processes. Inspired by these observations, we set out to create a modern analog of this material and explore its properties. Considering the relatively even distribution of the lime clasts and their well-defined morphologies, these observations raise the intriguing proposition that they may have been added to the concrete mix in their intact form (a practice known as hot mixing). Considering the documented use of hot mixing in both ancient and modern mortar preparations (*19*, *44*), we explored this approach in our synthetic formulations.

In our modern cementitious formulations, we combined OPC, pulverized fly ash, sand, and water at a mass mixing ratio of ca. 1:0.2:2:1. To this mixture (known herein as Mix 1), quicklime was added to different samples, spanning a concentration varying from 7.5 to 15 mass % (which was chosen on the basis of the encountered frequency range of relict lime clasts in different Roman concrete samples) to investigate the effects of quicklime content on the concrete's performance. The resulting mixtures were cast into cylindrical molds measuring 10 cm in diameter and 10 cm in height and cured under water for 28 days before use.

Once the production of our modern concrete samples was complete, we explored the microarchitecture of the lime clasts and compared their features to those found in their ancient Roman equivalents (Fig. 4). In both types of samples (ancient and modern), the bright white color of the lime clasts and their porous microstructure were visible. Further examination of the lime clasts from the polished samples of the Roman-inspired concrete formulations using polarized optical microscopy revealed a similar visibly distinctive periphery that was seen in the native Roman material (cf. Figs. 2F and 3E and figs. S7 to S9).

The potential for the high–surface area lime clasts to act as a reactive calcium source for self-healing properties was further investigated using our Roman-inspired concrete formulations. The cured samples were fractured by splitting the sample longitudinally (Fig. 5A), and the opposite walls of the cracked sample were adjoined at a distance of ca. 0.5 mm.

After an initial preconditioning step (*45*), the re-mated sides of the test samples (which also included lime clast–free controls) were then introduced into a flow circuit (Fig. 5B) and subjected to a constant water flow. The flow rate over 30 days was then recorded using electronic flow meters with a precision of ±5 liters/hour. In these studies, a measured decrease in flow rate was predicted to correspond to potential self-healing (crack-filling) activity. Typical initial values of flow rates through open cracks ranged between 10 and 30 liters/hour and reduced over the course of 1 to 3 weeks depending on the crack geometry, to almost zero when the crack was eventually sealed (Fig. 5C). When the flow of water eventually stopped (and the flow rate was zero or at a negligible flow), the test was stopped, and the nature and distribution of secondary products formed in the crack (Fig. 5, D to F) during the process were evaluated using optical microscopy (Fig. 5, D and E) and Raman spectroscopy (Fig. 5F).

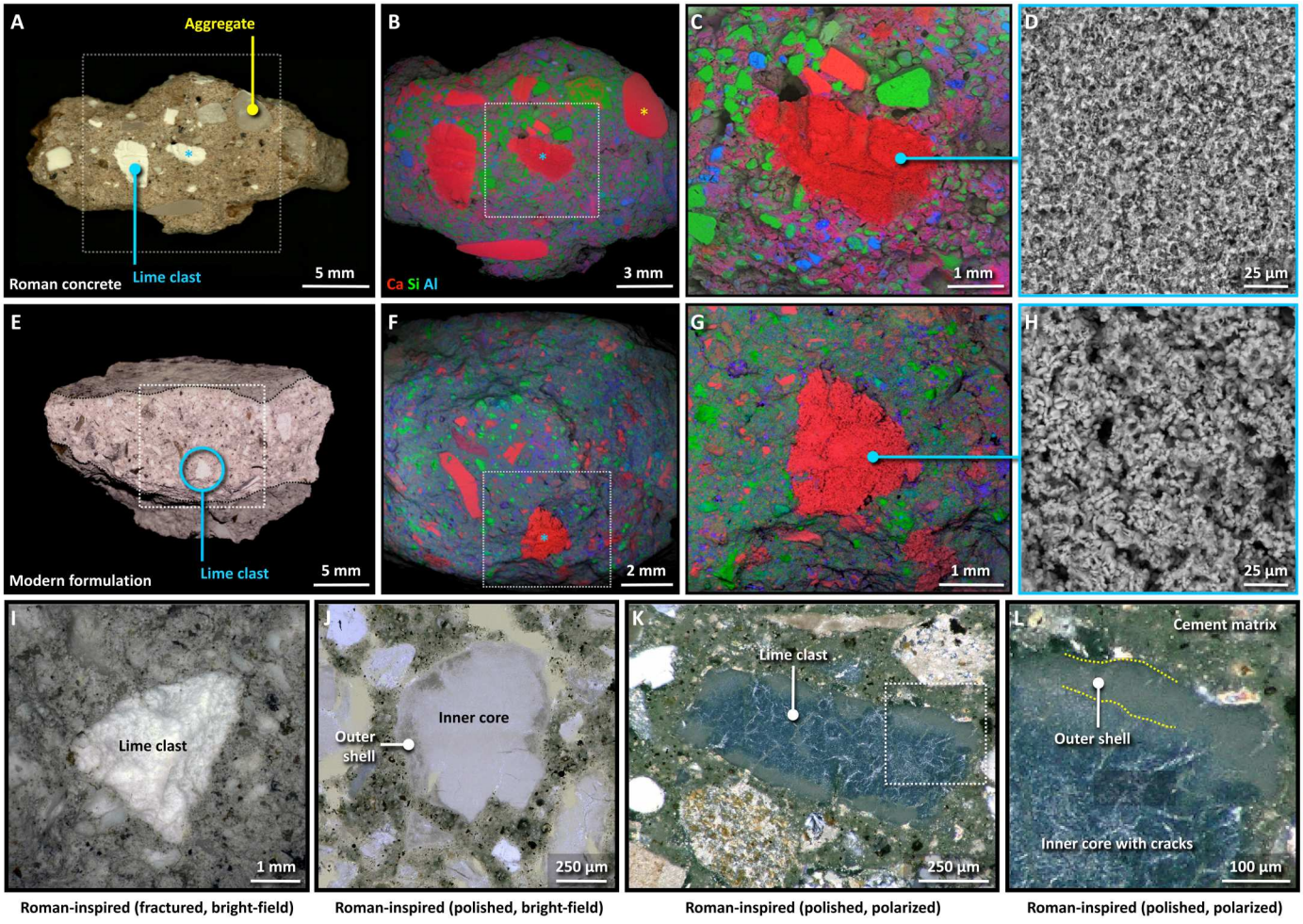

Fig. 4. Compositional and morphological characterization of ancient and modern lime clasts. (**A** and **E**) Optical micrographs showing the conspicuous bright white color of the lime clasts, which can easily be identified from large-area elemental mapping via SEM-EDS (**B**, **C**, **F**, and **G**), are morphologically distinct from other calcareous aggregate material (denoted by a yellow asterisk) and exhibit a distinctive particulate microstructure (**D** and **H**). The dotted boxes in (B) and (F) denote the locations of the magnified views in (C) and (G), respectively. (**I**) A higher magnified view of a single fractured lime clast from our hot-mixed Roman-inspired concrete formulation. The visibly distinguishable periphery of these lime clasts [denoted by the "outer shell" labels in (**J**) and (**L**)] can be easily seen via both bright-field and polarized illumination of polished samples, while polarized illumination specifically emphasizes the high density of internal cracking in the clasts (K and L). The dotted box in (**K**) denotes the location of the magnified views in (L).

On the basis of these initial findings and to assess the real-world applicability of a self-healing Roman-inspired quicklime-containing concretes in the modern built environment, we developed a second formulation (known herein as Mix 2) using an industrially relevant concrete recipe that included coarse aggregates and superplasticizer. These concrete samples (along with quicklime-free controls) were cast as rectangular prisms, and their drying shrinkage was measured 90 and 365 days after casting. After 90 days, the quicklime-containing Mix 2 concrete samples had shrunk 9% less than that of the quicklime-free controls, demonstrating the role of quicklime as an effective shrinkage compensator during the early stages of the curing process. At 365 days after casting, the drying shrinkage of the two concretes had converged (<1% difference), thus confirming the marginal effects of expansive quicklime in this industrially relevant concrete mix.

DISCUSSION

Previous evidence suggests that in ancient Roman cementitious structures, the relict lime clasts can react over time with other mortar components, forming both amorphous (C-A-S-H) and crystalline (e.g., Al-tobermorite and strätlingite) phases (*11*). These maturation pathways, however, are not the only ones observed in Roman cementitious materials and, as shown here, can also follow different trajectories depending on the local environmental conditions (Figs. 2 and 3). While the polished cross-sections of the ancient Roman concrete samples described in the present study (Fig. 2, D to F) do show clear inclusion of silicon and aluminum in the lime clast, suggesting that some conversion to C-A-S-H and/or its crystalline homologues occurred, calcium carbonate, predominantly as calcite, remains within their cores (Fig. 3D).

It has already been suggested that calcium carbonates originating from different sources (e.g., carbonated slaked lime, carbonated free lime, or geologic calcite) show differences in their morphology and

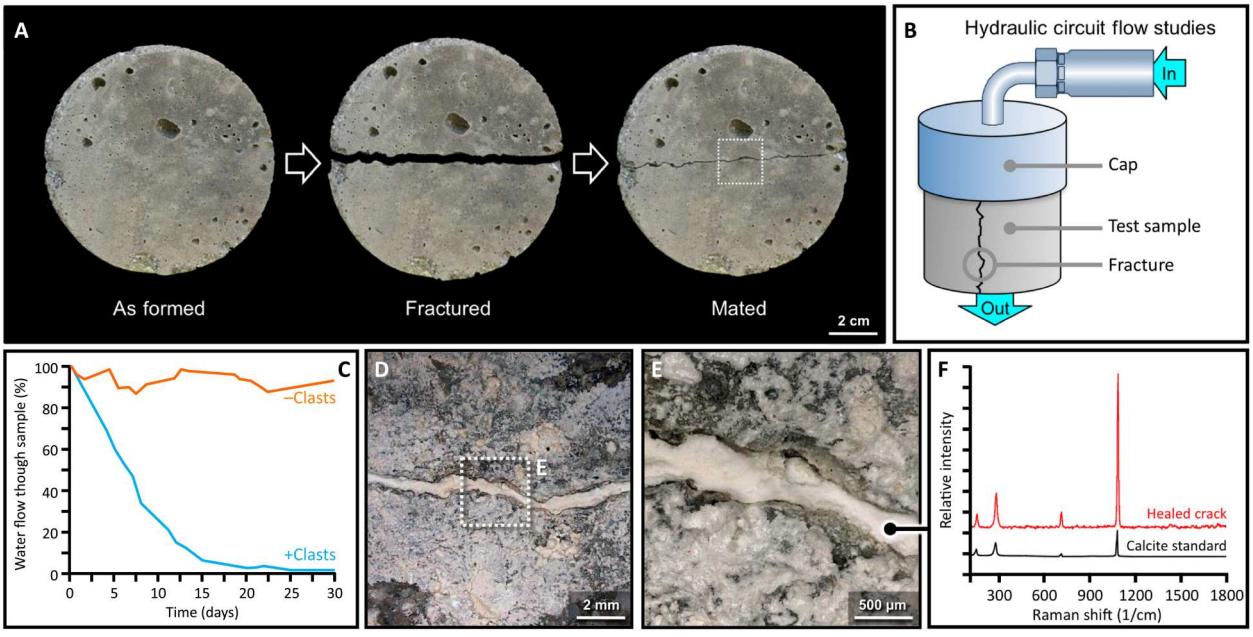

Fig. 5. Modern mortar self-healing experiments. After casting, the Roman-inspired hot-mixed concrete samples were mechanically fractured and then re-mated (with a gap of 0.5 ± 0.1 mm) and preconditioned for our crack-healing studies (**A**). Using an integrated flow circuit (**B**), water flow through the sample over the course of 30 days was documented with a flow meter. Compared to the lime clast–free control (orange line), after 30 days, water flow through the lime clast–containing sample (blue line) ceased (**C**), and examination of the cracked surface revealed that it had been completely filled with a newly precipitated mineral phase (**D** and **E**), which was identified as calcite from Raman spectroscopy measurements (**F**).

crystal structure (*46*, *47*). For example, slaked lime [$Ca(OH)_2$] transforms into calcite ($CaCO_3$) when exposed to atmospheric CO_2; however, it is relatively more disordered than geologic calcite samples and, for this reason, can, in some cases, be differentiated as such (*46*).

During the production of concrete, water availability plays a critical role in dictating the reaction kinetics and the evolution of different mineral phases. For example, previous Raman spectroscopy and XRD studies investigating the hydration and carbonation of calcium oxide samples exposed to different ambient humidity levels demonstrated that at relative humidities below 20%, calcium oxide converts to amorphous calcium carbonate (*48*). However, at relative humidity levels of 20 to 40%, conversion to calcite, aragonite, and vaterite was observed, while samples exposed to humidity levels above 60% showed only calcite. These results suggest that the relative humidity of the calcium oxide maturation environment can be inferred through the measurement of calcium carbonate polymorph ratios within the lime clasts.

Using these criteria and on the basis of the lime clast composition from ancient Roman concretes reported here, a potentially valid explanation of these water-depleted conditions could be hot mixing, referred to as such because of the exothermic nature of the CaO hydration reaction (*19*). In these preparations, quicklime is simultaneously mixed with the pozzolans, aggregates, and water instead of, or in addition to, slaked lime as the calcium source in the mortar. Hot mixing thus has the potential to change the conditions under which the lime clasts are transformed within the mortar. It is known that hot mixing of other ancient lime-based mortars is one method that leads to lime inclusions and that modern reproductions of these mortars have been shown to set faster compared to those made using slaked lime putty or powder (*18*, *19*). The characteristic features of the lime inclusions described in the present study could also be explained by the temperature increase associated with hot mixing, which facilitates both the reactions responsible for hardening the mortar and the formation of a gradient in hydration around the lime clasts, preventing them from further dissolution in the mortar matrix.

Regarding the production processes that may have favored the lime clasts remaining intact instead of dissolving and reacting in the binding matrix, previous research on other ancient Roman mortars has suggested a series of hypotheses. These possibilities include (i) hydration and subsequent partial carbonation of the lime before incorporation in the mortar; (ii) overburned lime, wherein the CaO is passivated and less reactive; (iii) underburned lime, wherein the lime is not completely calcined; or (iv) the use of coarse quicklime instead of a fine powder or paste (*18*, *30*). The gradient in composition seen in the EDS maps of the lime clasts in the Privernum samples suggests that some hydration-driven reactions have taken place between the lime and aluminosilicates in the binder, thus likely resulting from one of the latter two pathways. The use of coarse particles of quicklime (alone or in conjunction with slaked lime) in the mortar is another possibility, which could allow hydration reactions to take place on the clast exterior and allow the development of the chemical gradient seen in the lime clasts of the Privernum mortar and elsewhere (*5*, *12*, *32*, *49*). The heat resulting from the hydration of quicklime could reduce the availability of water, potentially resulting in the low-humidity conditions that could explain the Raman spectra reported here. Furthermore, these lime clast hydration gradients are also observed in our modern quicklime-containing mixes that were developed and

investigated in the present study (Fig. 4, J to L, and fig. S9). Further evidence supporting the hypothesis of quicklime use in the primary mix is the cracks observed in petrographic photomicrographs that form during the hydration of quicklime in both ancient samples (*12*) and modern reproductions (Fig. 4L), as well as the highly porous nature of lime clasts observed in the fractured surfaces of both ancient and modern lime inclusions (Fig. 4, D and H).

Both of these phenomena (the formation of internal microcracks and a porous architecture) can be attributed to volume changes associated with lime cycle transformations. The CaO reaction with water to produce $Ca(OH)_2$ is accompanied by a density-induced volume expansion of ca. 33% (assuming the densities of CaO and $Ca(OH)_2$ at 3.34 and 2.2 g/cm^3, respectively) and accounts for clast crack formation and the observed porosity. While these volumetric changes in the concrete constituents might be expected to negatively affect concrete performance, our results with modern lime clast–containing industrially relevant concrete formulations have demonstrated that, even after 1 year, lime clast–containing concretes exhibit negligible drying shrinkage compared to their lime clast–free controls.

Despite extensive literature related to the composition and applications of ancient Roman concretes, the exact order of operations for Roman mortar production based on historical evidence remains ambiguous. There is even debate as to whether preparation techniques differed between the production of marine and terrestrial cementitious structures (*12*). Imperial age mortar (according to Vitruvius) was prepared by mixing lime with volcanic sand (materies ex calce et harena mixta). During the Republican period, Cato, in his De Agri Cultura (*50*), describes the mortar mix as calx harenatus ("lime with sand"). The wet mortar mix would then be mixed with tuff and brick caementa to form a concrete. In general, for frescoes and wall plaster, for example, the ancient scholars would often suggest the aging of lime in water before use and ensure that it was as finely ground as possible (*17*), because incompletely hydrated lime particles, known as bottaccioli in these applications, could absorb water over time and expand, damaging the paint (fresco) layer. For this reason, both Vitruvius (*6*) and Pliny (*17*) describe the preparation of lime for plasterwork to involve a thorough soaking or softening process (macerata). When referring to lime for structural use, however, Vitruvius uses the word extincta (II.5.1) instead of macerata. While extincta and macerata are both frequently interpreted as referring to slaking, Vitruvius' change in diction points to a potentially different process. On the basis of the results of our chemical characterization of the Privernum mortars, it is thus possible that in contrast to the use of macerata (which specifically refers to the slaking process), extincta could refer to lime hydrated simultaneously with the other mortar components, supporting the hot mixing hypothesis proposed here. Furthermore, it has also been previously proposed that some Roman mortars were prepared through the sequential addition of both slaked lime and quicklime in a two-step process (*51*).

Hydration of quicklime during hot mixing produces an exothermic reaction as CaO hydrates to form $Ca(OH)_2$. The temperature increase in the mortar is approximately 55° to 60°C over ambient (*52*), with a presence of hot spots characterized by temperatures exceeding 200°C (*19*). Previous thermodynamic modeling of the pozzolanic (hydration) reaction in Roman marine concrete has suggested that temperatures up to 97°C are possible within thick concrete structures from the pozzolanic reaction alone (*23*). The heat from these two reactions, the hydration of CaO and the pozzolanic reaction, could facilitate the formation of C-A-S-H and even crystalline phases such as Al-tobermorite and strätlingite, in the

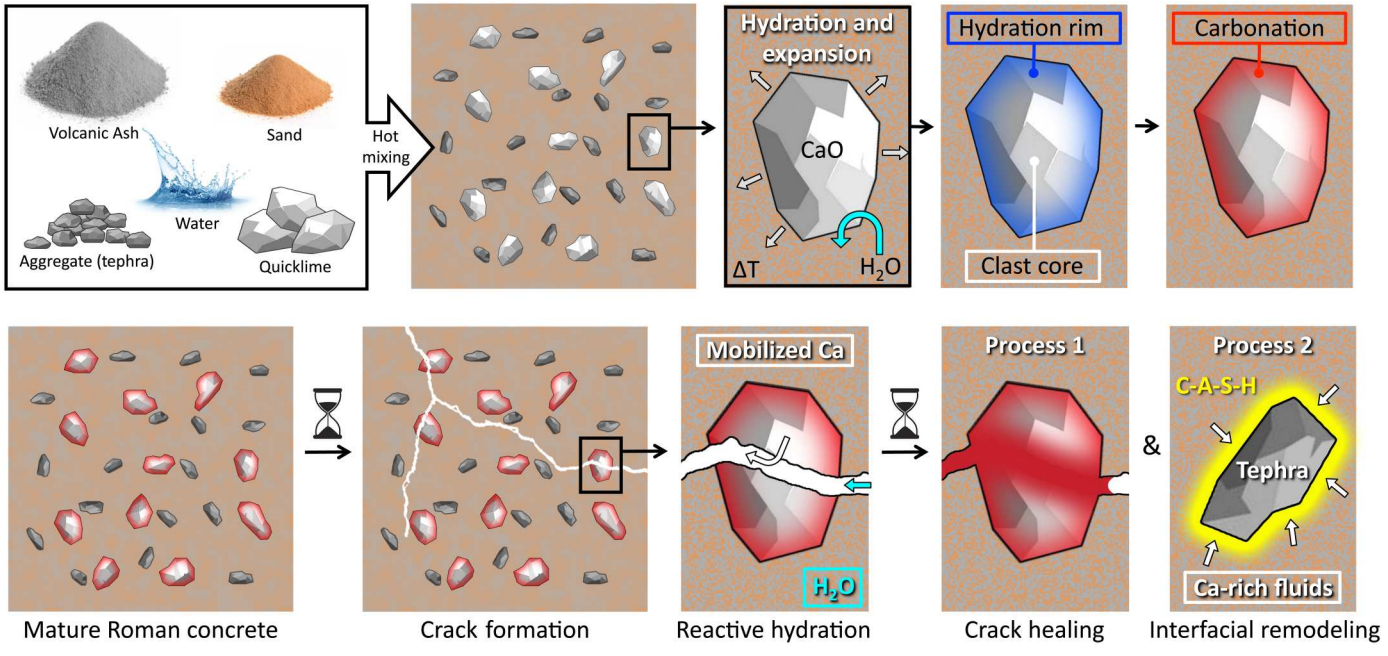

Fig. 6. Schematic of the proposed mechanism for self-healing within ancient Roman mortars. Through the process of hot mixing, the calcium-rich lime clasts are encapsulated by the cementitious matrix, which, following the formation of a hydration rim, ultimately undergo carbonation (top row). Upon cracking (bottom row), water can infiltrate, transporting a calcium-enriched solution into the pore network to heal the damage (process 1) or serve as reactive calcium for post-pozzolanic reactions (such as C-A-S-H formation) at the interface between the volcanic tephra and the surrounding matrix (process 2).

cementing matrix and along the reaction rim of the lime clasts in the early stages of the mortar hydration. Evidence for these reactions is further supported by the inclusion of silicon and aluminum in the EDS clusters identified within the reaction rims of the lime clasts studied herein and several pieces of evidence reported elsewhere (*34*). The pozzolanic reaction is sensitive to changes in temperature (*39*), and, hence, hot mixing provides a plausible explanation for the gradient in composition seen within the lime clasts of the Privernum mortar samples described in the current work and those from other Roman concretes (*12*, *32*).

Whereas previous evidence supports the formation of Al-tobermorite minerals in lime clasts of maritime structures due to the heat of the pozzolanic reaction (*23*), the results presented here suggest that, by contrast, when quicklime is introduced via hot mixing in terrestrial structures, the reaction is limited to the outer rim of the lime clast, encapsulating calcium-rich core structures within mortar matrix. This particular configuration can be observed in the comparison of Roman and modern samples (Figs. 2 and 4), both showing the same type of lime clast inclusions, hydration-driven cracking, and distinctive reaction rims. The initially matrix-incorporated clasts would then undergo a slow transformation into calcium-rich, highly porous phases of various polymorphs of calcium carbonate.

Inspired by these discoveries, it is thus likely that the high abundance of aggregate-scale lime clasts in ancient Roman mortars could thus serve as a source of calcium for post-pozzolanic processes in a pore- and crack-filling "self-healing" mechanism that combats the progressive degradation of these cementitious materials (Fig. 6). Over time, as cracks and pores form, the intrusion of water causes the dissolution of calcium-based phases in the relict lime clasts carrying them into the pore network. As the calcium-rich fluids leach into the cracks or the connected pore network, many pathways exist for potential post-pozzolanic reactions. For example, excess pozzolanic material, such as volcanic ash that did not react during the initial setting and curing, or aggregates of volcanic origin, can now dissolve and react with Ca-rich fluids originating from the lime clasts to form C-A-S-H phases, thus reinforcing the interfacial zones between volcanic aggregates/ash and the binding matrix (*29*). This strengthening is associated with the consolidation of the interfacial zones and increased mechanical performance of the C-A-S-H compared to its precursors (*53*). Another possible pathway is the recrystallization of $CaCO_3$ phases within the pore/crack space. This pathway, in which secondary calcium carbonate is precipitated through a mechanism similar to the one occurring in the formation of calthemites (*54*, *55*), relies on the wetting and drying cycles experienced through normal weathering conditions. These processes have been observed previously in both modern and ancient carbonate-based mortars (*56*–*58*). In contrast to these previous studies, however, we suggest here that the hot mixing–transformed lime clasts act as a calcium source for these processes and, furthermore, the precipitation of calcium carbonate as a crack-filling mechanism is already a known pathway for autogenous healing in other ancient lime-containing mortars (*57*). In the present study, we demonstrate the calcium enrichment of matrix phases adjacent to the lime clasts (shown in red in Fig. 2F), supporting the hypothesis that the lime clasts are a source of calcium for leaching and recrystallization within the pore space of the mortars (Fig. 2, D to F). Microcrack filling by calcite has been recently observed in ancient Roman mortars from the tomb of Caecilia Metella (*29*), and the self-healing tests carried out on our modern samples described in the present study (Figs. 4 and 5, C to F) further support this hypothesis.

An important question to be asked at this point is how the gradual carbonation of lime clasts affects the self-healing capacity of the final mixes. It is clear that the freshly hot-mixed concrete that incorporates lime clasts has autogenous self-healing potential. If a crack propagates through the concrete, then the high–surface area $Ca(OH)_2$-rich clasts release Ca^{2+} into a highly alkaline solution that readily carbonates and seals the crack (Fig. 5). A long-term carbonation of clasts would intuitively compete with this process considering the buffering effect of carbonates and subsequent pH reduction of the fluid that is oversaturated in chemical constituents. Nevertheless, in the case of lime clast carbonation [a process that is distinct from the carbonation of portlandite in modern concrete formulations (*59*)], a high surface area (evident in SEM images) further improves solubility (*60*), thus benefiting the mechanism proposed herein.

The proposed post-pozzolanic process introduced here can be compared to the autogenous healing in modern cementitious materials wherein cracks are filled by carbonation products or via the further hydration of unreacted pozzolanic particles (*61*, *62*). It should be noted that cementitious compounds contained in the concrete can always induce some degree of natural self-healing. For example, it is generally assumed that in these types of self-healing studies, where water is pumped through a damaged structure, at relatively low–water pressure gradients and up to 10% relative movement of the crack, any crack with a width of up to 0.20 mm can naturally self-heal, while for relative movements between 10 and 20%, the crack width for natural self-healing is between 0.15 and 0.20 mm (*63*). However, for cracks wider than the above values (such as those used for the self-healing experiments in Fig. 5), any measured reduction in water flow through the structure induced by self-healing would imply that additional mechanisms have occurred.

The effectiveness of the pore- and crack-filling mechanism described here is predicated on the frequency of cracks intersecting the abundant highly porous and intrinsically reactive lime clasts. In support of this requisite damage mode, the optical and SEM imaging of freshly fractured ancient Roman concrete surfaces reveals that fractures predominantly propagate through the lime clasts in the architectural mortar, which are visible on both sides of the crack interface. It should be noted, however, that lime production in antiquity could lead to underburned/overburned lime that could potentially influence their surface area, subsequent reactivity, and mechanical properties. While our analyses suggest that lime clast composition in Roman mortars is relatively consistent from sample to sample, in some cases, higher-density lime clasts in ancient mortars can act as aggregate, with cracks instead propagating through the interfacial transition zone (*5*).

The entire self-healing mechanism suggested here occurs upon stimulation from external forces that would, otherwise, cumulatively result in material failure if left unchecked. The calcium-rich phases within the lime clasts remain stored until they are needed, thus potentially allowing the healing properties of these materials to persist over millennia. To this end, microcracks and pores induced by environmental changes (e.g., freeze-thaw cycling and acid rain) or mechanical damage (e.g., settling and seismic loads) can be filled, with water activation, once the cracks reach the lime clast particles.

In this work, we successfully demonstrate that these ancient concrete design practices could be applied for the development of modern OPC-based formulations, thus showing far-reaching implications for extended concrete design life, long-term durability, and sustainability. Whether the damage occurs within years of construction or centuries thereafter, so long as the lime clasts remain, these self-healing functionalities can persist. Inspired by the demonstrated potential of this technology, future studies will explore how such an ad hoc self-healing mechanism can be implemented in modern infrastructure, both for reinforced concrete and for unreinforced applications as are commonly used, for example, in concrete three-dimensional printing efforts (*64*).

MATERIALS AND METHODS

Experimental design

The following analytical methods were carried out to (i) investigate the multiscale compositional heterogeneity of ancient Roman mortars and (ii) to extract the design principles for the development and testing of modern Roman-inspired concrete formulations.

Sample collection

Samples were collected during the summer of 2016 from bedding mortar in the masonry of the city wall at the Privernum archaeological site, near Rome, Italy, and stored under ambient conditions. The analyses described here were performed on 10 different samples from the Privernum archaeological site, and the results are representative of the trends observed.

Roman-inspired concrete samples

In this study, we investigated two Roman-inspired concrete formulations (Mix 1 and Mix 2). Mix 1 (a coarse aggregate–free mortar that was used in our self-healing experiments) consisted of OPC, pulverized fly ash, sand, and water, at a ratio of (1:0.2:2:1). To this mixture, quicklime was incorporated, spanning concentrations varying from 7.5 to 15 mass %. To evaluate the effects of quicklime addition on a representative industrially relevant concrete formulation, we prepared Mix 2, which consisted of OPC, pulverized fly ash, sand, water, superplasticizer, and coarse aggregate at a ratio of (1:0.4:2.5:0.7:0.01:3). To this mixture, quicklime was incorporated as a partial substitution of aggregates at a concentration of 4.3 mass %.

The compositional details of each of these components are as follows: OPC was CEM I 42.5 and conformed to EN 197-1 (OPC type I of ASTM 150); fly ash conformed to EN 450-1 (class F of ASTM C680); sand conformed to EN 12620 (or ASTM C33); coarse aggregate conformed to EN 12620 (or ASTM C33); superplasticizer was Masterglenium Sky 799; water conformed to EN 1008; and quicklime (with particle sizes of <4 mm) exhibited a CaO content above 96.9%. The self-healing experiments and the mortar formulations (the Mix 1 samples and their quicklime-free controls) were cast into cylindrical molds measuring 10 cm in diameter and 10 cm in height and cured under water for 28 days before use. The industrially relevant concrete formulations (the Mix 2 samples and their quicklime-free controls) were cast as rectangular prisms measuring 360 mm in length, 120 mm in width, and 120 mm in height. To determine the volumetric stability of the Mix 2 concrete sample, drying shrinkage was measured in accordance with the Swiss norm SIA 2621/F protocol, after 90 and 365 days.

Scanning electron microscopy and energy dispersive x-ray spectroscopy

Elemental analysis to complement the microstructural data was obtained using quantitative SEM-EDS. Element mapping was used to study the composition and the spatial distribution of phases within the mortar, specifically the lime clasts and the surrounding matrix, and its chemistry was investigated on both polished and freshly fractured surfaces. The latter was included to avoid potential artifacts from the sample preparation process, such as chemical alteration of the lime clasts (e.g., carbonation) during the polishing process. The scanned areas were selected on the basis of the presence of lime clasts within the section. Polished samples were embedded and prepared by a commercial third party, and the fractured surfaces were exposed immediately before sample mounting and imaging.

All samples were imaged (uncoated) in low vacuum (15 Pa) with an acceleration voltage of 20 keV using a Tescan Vega GMU scanning electron microscope. The fracture surface measurements were acquired using a Bruker dual-detector EDS system to minimize shadowing artifacts. The pixel size for the EDS data was adjusted to correspond to the estimated interaction volume, in this case ca. 3 μm, so that overlap of data did not interfere with the interpretation of phases present. Each pixel in the elemental map contained an EDS spectrum corresponding to the 3-μm pixel area. The quantification was performed using 2 × 2 binning that aggregates the counts in a 2 pixel–by–2 pixel area before quantifying the elemental composition. Quantification of the binned EDS data was performed using Bruker′s Esprit 2.1 software with the built-in Linemarker PB-ZAF correction. This correction accounts for background radiation, atomic number effects, absorption of x-rays by the specimen, and fluorescence. Individual EDS maps showing the atomic percent of each element (e.g., calcium and silicon) present at each 3 μm–by–3 μm pixel were then extracted. The quantified EDS maps were processed using custom MATLAB scripts (*41*) to convert the pixels into matrices where each entry represents the atomic percent of calcium, silicon, magnesium, aluminum, oxygen, or other elements present in each pixel. The relative ratios of these elements of interest were plotted as ternary diagrams.

Each EDS dataset was visualized using fuzzy *c*-means clustering (Fuzzy Logic Toolbox, MATLAB R2018a). Fuzzy clustering differs from hard clustering in that each data point may be a part of multiple clusters. This assumption holds for this purpose, because a given 3 μm–by–3 μm pixel of the measured area may encompass more than one phase. Data points were ultimately divided into clusters using the highest membership value for each data point. Using this technique, each dataset was divided into clusters, and the number of clusters was increased until the map was appropriately segmented. Clustering was performed on an *n*-by-5 array of EDS data, where *n* is equal to the number of pixels in the EDS map of interest, and each column contained the quantity of each of the five elements of interest (oxygen, silicon, calcium, magnesium, and aluminum) in atomic percent.

Powder x-ray diffraction

XRD samples were prepared by extracting visible lime clasts from mortar samples. After lime clast extraction, the remaining matrix was manually scraped from the sample to reduce the potential for cross-contaimation. Samples were then ground to a fine powder using an agate mortar and pestle no more than 24 hours before data acquisition.

Powder XRD was performed in the X-Ray Diffraction Facility at the Center for Materials Science and Engineering at the Massachusetts Institute of Technology. Diffraction data were collected with a PANalytical X′Pert Pro diffractometer using copper Kα radiation in a Bragg-Brentano geometry. The scans were performed from 10° to 90° 2θ at increments of 0.008. Each increment was acquired for 50.165 s. Powder XRD phase identification was performed with the HighScore Plus software using the ICDD PDF-4 database.

Raman spectroscopy

Raman spectroscopy was performed with a WiTec Alpha 300R confocal Raman microscope. The spectra were acquired with a thermoelectrically cooled charge-coupled device detector (DU401A-BV, Andor, UK) placed behind a grating (600 g/mm) spectrograph (UHTS 300, WITec, Ulm, Germany) with a spectral resolution of 3 cm^{-1}. A Research Electro-Optics 35-mW helium-neon 633-nm laser was used at 33% power to collect Raman spectra from the lime clasts. A Zeiss EC Epiplan-Neofluar 100× [numerical aperture (NA), 0.9] objective lens was used for imaging, and the spectra were collected for 1.0 s per point. The 400 μm–by–400 μm area presented in Fig. 3E and fig. S4 was divided into a 250-by-250 grid, for a total resolution of 1.6 μm per pixel. The 300 μm–by–300 μm area in fig. S5 was divided into a 120-by-120 grid for a resolution of 2.5 μm per pixel. The Raman map shown in fig. S2 and spectra used for calculating the peak widths in fig. S6 were collected using a Research Electro-Optics 75-mW 532-nm laser at 25% power and a Zeiss LD EC Epiplan-Neofluar 50× (NA, 0.55) objective lens. The Raman map in fig. S2 was generated from spectra collected for 0.6 s each, at a spatial resolution of 4 μm per pixel over the 200 μm–by–200 μm scan area. Single-point spectra of various lime inclusions were collected for 1.0 s each for fig. S6. Using a 532-nm laser, only the υ_1 carbonate peak was detectable above the fluorescence signal in the lime inclusions. All spectra used a grating at 600 g/mm for data collection.

Processing of the Raman data was done using WiTec's Project 5 software. Background subtracted spectra were identified using the built-in *k*-means clustering function. Known spectra (e.g., resin, calcite, and quartz) identified with the *k*-means clustering were subtracted from the rest until distinct spectra remained (demixing). The spectra presented here are the demixed average spectra of the identified clusters. Raman maps were created in WiTec Project 5 showing the intensity of the identified component spectra in the background-subtracted scan data. Color intensity is proportional to the intensity of the component spectrum's intensity at that point, and color mixing indicates that the spectrum at that point is a combination of component phases.

Self-healing experiments

After mechanical fracturing, the re-mated sides of the test samples (and lime clast–free controls) were introduced into a flow circuit (Fig. 5B) and subjected to a water flow that was constantly measured to confirm the consistency of the crack. The self-healing experiments consisted of four sequential experimental phases: (i) specimen preparation, (ii) crack validation, (iii) specimen preconditioning, and (iv) crack healing.

These experimental phases are reported as follows:

1) Specimen preparation: After casting, the cylindrical test samples were cured underwater at room temperature for 28 days before being split longitudinally. After air drying, the two halves of each test sample were rejoined with an interior crack spacing of 0.5 ± 0.1 mm and introduced into a metered flow circuit.

2) Crack validation: To verify the intact nature of the cracks for the mounted samples, water was pumped through the flow circuit equipped with electronic flow meters with a precision of ±0.5 liters/hour, before any preconditioning or crack healing measurements were performed. A continuous, uninterrupted flow of water through the test sample was used to verify the crack's dimensional stability.

3) Specimen preconditioning: To discriminate between intrinsic small crack healing mechanisms for sub–0.2-mm-wide cracks, which have been reported previously for most concrete formulations (*45*) and other potential large-scale self-healing mechanisms, the samples were first subjected to a 2-month-long period of sequential wet/dry cycling, as described previously (*45*).

4) Crack healing: After the initial preconditioning step, the samples were subjected to a continuous source of water flow over the course of 30 days. In these studies, a measured decrease in flow rate (compared to that of the lime clast–free controls) was predicted to correspond to potential self-healing (crack-filling) activity.

Petrographic analysis

Petrographic analysis was performed using a Keyence VHX-950F digital microscope on polished thin sections measuring ca. 25 μm in thickness to examine the mineralogy of the filled cracks, the lime clasts, and the surrounding matrix material.

Supplementary Materials

This PDF file includes:

Supplementary Text
Figs. S1 to S9

REFERENCES AND NOTES

1. J. Allwood, J. Cullen, Sustainable Materials With Both Eyes Open (UIT Cambridge, 2011).
2. J. R. Mackechnie, M. G. Alexander, Using durability to enhance concrete sustainability. *J. Green Build.* **4**, 52–60 (2009).
3. L. Bertrand, C. Gervais, A. Masic, L. Robbiola, Paleo-inspired systems: Durability, sustainability, and remarkable properties. *Angew. Chem. Int. Ed. Engl.* **57**, 7288–7295 (2018).
4. K. T. Faber, F. Casadio, A. Masic, L. Robbiola, M. Walton, Looking back, looking forward: Materials science in art, archaeology, and art conservation. *Annu. Rev. Mat. Res.* **51**, 435–460 (2021).
5. A. Palomo, P. Monteiro, P. Martauz, V. Bilek, A. Fernandez-Jimenez, Hybrid binders: A journey from the past to a sustainable future (opus caementicium futurum). *Cem. Concr. Res.* **124**, 105829 (2019).
6. V. Pollio, F. Granger, *British Library. Harley 2767, On architecture* (Harvard Univ. Press, 1931).
7. C. G. Malacrino, *Constructing the Ancient World: Architectural Techniques of the Greeks and Romans* (J. Paul Getty Museum, 2010).
8. L. C. Lancaster, Mortars and plasters—How mortars were made. The literary sources. *Archaeol. Anthropol. Sci.* **13**, 192 (2021).
9. M. Jackson, D. Deocampo, F. Marra, B. Scheetz, Mid-Pleistocene pozzolanic volcanic ash in ancient Roman concretes. *Geoarchaeology* **25**, 36–74 (2010).
10. F. Massazza, M. Pezzuoli, Some teachings of a Roman concrete, in *Mortars, Cemeilts and Grouts Used in the Conservation of Historic Buildings* (ICCROM, 1981), pp. 219–245.
11. M. D. Jackson, S. R. Mulcahy, H. Chen, Y. Li, Q. Li, P. Cappelletti, H.-R. Wenk, Phillipsite and Al-tobermorite mineral cements produced through low-temperature water-rock reactions in Roman marine concrete. *Am. Mineral.* **102**, 1435–1450 (2017).
12. M. D. Jackson, G. Vola, E. Gotti, B. Zanga, Sea-water concretes and their material characteristics, in Building for Eternity: The History and Technology of Roman Concrete Engineering in the Sea, J. P. Oleson, Ed. (Oxbow Books, 2014), pp. 141–188.

13. G. Artioli, M. Secco, A. Addis, The Vitruvian legacy: Mortars and binders before and after the Roman world, in *The Contribution of Mineralogy to Cultural Heritage* (Mineralogical Society of Great Britain and Ireland, 2019), pp. 151–202.
14. J. P. Oleson, L. Bottalico, C. Brandon, R. Cucitore, E. Gotti, R. L. Hohlfelder, Reproducing a Roman maritime structure with Vitruvian pozzolanic concrete. *J. Roman Archaeol.* **19**, 29–52 (2006).
15. R. L. Hohlfelder, C. Brandon, P. Oleson, Building a Roman *Pila* in the sea—Experimental archaeology at Brindisi, Italy, September 2004. *Int. J. Naut. Archaeol.* **34**, 123–127 (2005).
16. H. Lechtman, L. Hobbs, W. D. Kingery, Roman concrete and the roman architectural revolution, in *Ceramics and Civilization, Volume 3: High Technology Ceramics: Past, Present, Future* (American Ceramics Society, 1986), vol. 3, pp. 81–128.
17. Pliny, D. E. Eichholz, *Natural History, Volume X: Books 36–37* ([electronic resource] translated by D.E. Eichholz, Harvard Univ. Press, 1962).
18. A. B. Leslie, J. J. Hughes, Binder microstructure in lime mortars: Implications for the interpretation of analysis results. *Q. J. Eng. Geol. Hydrogeol.* **35**, 257–263 (2002).
19. A. Forster, Hot-lime mortars: A current perspective. *J. Archit. Conserv.* **10**, 7–27 (2004).
20. J. Elsen, Microscopy of historic mortars—A review. *Cem. Concr. Res.* **36**, 1416–1424 (2006).
21. J. Valek, A. Zeman, Characteristics of lime particles in hot mixed mortars, in *Proceedings of the 12th Euroseminar on Microscopy Applied to Building Materials* (Dortmund, 2009).
22. L. M. Seymour, D. Keenan-Jones, G. L. Zanzi, J. C. Weaver, A. Masic, Reactive ceramic aggregates in mortars from ancient water infrastructure serving Rome and Pompeii. *Cell Rep. Phys. Sci.* **3**, 101024 (2022).
23. D. Jackson Marie, R. Chae Sejung, R. Mulcahy Sean, C. Meral, R. Taylor, P. Li, A.-H. Emwas, J. Moon, S. Yoon, G. Vola, H.-R. Wenk, J. M. Monteiro Paulo, Unlocking the secrets of Al-tobermorite in Roman seawater concrete. *Am. Mineral.* **98**, 1669–1687 (2013).
24. M. D. Jackson, E. N. Landis, P. F. Brune, M. Vitti, H. Chen, Q. Li, M. Kunz, H.-R. Wenk, P. J. M. Monteiro, A. R. Ingraffea, Mechanical resilience and cementitious processes in Imperial Roman architectural mortar. *Proc. Natl. Acad. Sci.* **111**, 18484–18489 (2014).
25. T. Vanorio, W. Kanitpanyacharoen, Rock physics of fibrous rocks akin to Roman concrete explains uplifts at Campi Flegrei Caldera. *Science* **349**, 617–621 (2015).
26. J. Elsen, O. Cizer, R. Snellings, Lessons from a lost technology: The secrets of Roman concrete. *Am. Mineral.* **98**, 1917–1918 (2013).
27. M. D. Jackson, G. Vola, D. Všianský, J. P. Oleson, B. E. Scheetz, C. Brandon, R. L. Hohlfelder, Cement microstructures and durability in ancient Roman seawater concretes, in *Historic Mortars* (Springer Netherlands, 2012), pp. 49–76.
28. M. Jackson, J. Oleson, J. Moon, Y. Zhang, H. Chen, M. Gudmundsson, Extreme durability in ancient Roman concretes. *Am. Ceram. Soc. Bull.* **97**, 22–28 (2018).
29. L. M. Seymour, N. Tamura, M. D. Jackson, A. Masic, Reactive binder and aggregate interfacial zones in the mortar of Tomb of Caecilia Metella concrete, 1C BCE, Rome. *J. Am. Ceram. Soc.* **105**, 1503–1518 (2022).
30. S. Bruni, F. Cariati, P. Fermo, P. Cairati, G. Alessandrini, L. Toniolo, White lumps in fifth- to seventeenth-century AD mortars from Northern Italy. *Archaeometry* **39**, 1–7 (1997).
31. J. Elsen, A. Brutsaert, M. Deckers, R. Brulet, Microscopical study of ancient mortars from Tournai (Belgium). *Mater Charact* **53**, 289–294 (2004).
32. G. Vola, E. Gotti, C. Brandon, J. P. Oleson, R. L. Hohlfelder, Chemical, mineralogical and petrographic characterization of Roman ancient hydraulic concretes cores from Santa Liberata, Italy, and Caesarea Palestinae, Israel. *Period Mineral.* **80**, 317–338 (2011).
33. E. Uğurlu Sağın, H. E. Duran, H. Böke, Lime mortar technology in ancient eastern Roman provinces. *J. Archaeol. Sci. Rep.* **39**, 103132 (2021).
34. M. D. Jackson, J. Moon, E. Gotti, R. Taylor, S. R. Chae, M. Kunz, A. Emwas, C. Meral, P. Guttmann, P. Levitz, Material and elastic properties of Al-tobermorite in ancient Roman seawater concrete. *J. Am. Ceram. Soc.* **96**, 2598–2606 (2013).
35. K. Celik, M. D. Jackson, M. Mancio, C. Meral, A.-H. Emwas, P. K. Mehta, P. J. M. Monteiro, High-volume natural volcanic pozzolan and limestone powder as partial replacements for portland cement in self-compacting and sustainable concrete. *Cem. Concr. Compos.* **45**, 136–147 (2014).
36. M. D. Jackson, J. M. Logan, B. E. Scheetz, D. M. Deocampo, C. G. Cawood, F. Marra, M. Vitti, L. Ungaro, Assessment of material characteristics of ancient concretes, Grande Aula, Markets of Trajan, Rome. *J. Archaeol. Sci.* **36**, 2481–2492 (2009).
37. L. C. Lancaster, Concrete Vaulted Construction in Imperial Rome. (Cambridge Univ. Press, 2005).
38. J. MacFarlane, T. Vanorio, P. J. M. Monteiro, Multi-scale imaging, strength and permeability measurements: Understanding the durability of Roman marine concrete. *Construct. Build Mater.* **272**, 121812 (2021).
39. F. M. Taylor, *Cement Chemistry* (Thomas Telford Publishing, ed. 2, 1997).
40. C. Carde, R. François, Modelling the loss of strength and porosity increase due to the leaching of cement pastes. *Cem. Concr. Compos.* **21**, 181–188 (1999).
41. J. M. Maragh, J. C. Weaver, A. Masic, Large-scale micron-order 3D surface correlative chemical imaging of ancient Roman concrete. *PLOS ONE* **14**, e0210710 (2019).
42. U. Wehrmeister, D. E. Jacob, A. L. Soldati, N. Loges, T. Häger, W. Hofmeister, Amorphous, nanocrystalline and crystalline calcium carbonates in biological materials. *J. Raman Spectrosc.* **42**, 926–935 (2011).
43. M. D. Jackson, G. Vola, Appendix 4: Compositional Analyses of Concretes Drilled from Harbour Structures by ROMACONS, in *Building for Eternity: The History and Technology of Roman Concrete Engineering in the Sea*, J. P. Oleson, Ed. (Oxbow Books, 2014), pp. 285–306.
44. C. Pesce, M. C. Godina, A. Henry, G. Pesce, Towards a better understanding of hot-mixed mortars for the conservation of historic buildings: The role of water temperature and steam during lime slaking. *Herit. Sci.* **9**, 72 (2021).
45. W. Zhang, Q. Zheng, A. Ashour, B. Han, Self-healing cement concrete composites for resilient infrastructures: A review. *Compos. Part B Eng.* **189**, 107892 (2020).
46. B. Xu, M. B. Toffolo, L. Regev, E. Boaretto, K. M. Poduska, G. Mor, L. Addadi, S. Weiner, Y. Politi, M. Goder-Goldberger, Structural differences in archaeologically relevant calcite. *Anal. Methods* **7**, 9304–9309 (2015).
47. K. M. Poduska, L. Regev, E. Boaretto, L. Addadi, S. Weiner, L. Kronik, S. Curtarolo, Decoupling local disorder and optical effects in infrared spectra: Differentiating between calcites with different origins. *Adv. Mater.* **23**, 550–554 (2011).
48. E. Dubina, J. Plank, L. Korat, J. Strupi-Šuput, L. Black, Influence of water vapour and carbon dioxide on free lime during storage at 80°C, studied by Raman spectroscopy. *Spectrochim. Acta Part Mol. Biomol. Spectrosc.* , 299–303 (2013).
49. L. Randazzo, M. Ricca, S. Ruffolo, M. Aquino, B. Davidde Petriaggi, F. Enei, M. F. La Russa, An integrated analytical approach to define the compositional and textural features of mortars used in the underwater archaeological site of Castrum Novum (Santa Marinella, Rome, Italy). *Minerals* **9**, 268 (2019).
50. M. P. Cato, A. Dalby, *On farming: De agricultura* (Prospect Books, 1998).
51. H. Jedrzejewska, New methods in the investigation of ancient mortars, in *Archaeological Chemistry: A Symposium*, M. Levey, Ed. (University of Pennsylvania Press, 1967), pp. 147–166.
52. J.-M. Commandré, S. Salvador, A. Nzihou, Reactivity of laboratory and industrial limes. *Chem. Eng. Res. Des.* **85**, 473–480 (2007).
53. M. J. Abdolhosseini Qomi, F. Ulm, R. J. Pellenq, Evidence on the dual nature of aluminum in the calcium-silicate-hydrates based on atomistic simulations. *J. Am. Ceram. Soc.* **95**, 1128–1137 (2012).
54. G. K. Smith, Calcite straw stalactites growing from concrete structures. *Cave Karst Sci.* **43**, 4–10 (2016).
55. P. L. Broughton, Morphogenesis and microstructure of concrete-derived calthemites. *Environ. Earth Sci.* **79**, 245 (2020).
56. H. Huang, G. Ye, C. Qian, E. Schlangen, Self-healing in cementitious materials: Materials, methods and service conditions. *Mater. Des.* **92**, 499–511 (2016).
57. B. Lubelli, T. G. Nijland, R. P. J. van Hees, Self-healing of lime based mortars: Microscopy observations on case studies. *Heron* **56**, 81–97 (2011).
58. D. Miriello, A. Bloise, G. M. Crisci, R. De Luca, B. De Nigris, A. Martellone, M. Osanna, R. Pace, A. Pecci, N. Ruggieri, New compositional data on ancient mortars and plasters from Pompeii (Campania – Southern Italy): Archaeometric results and considerations about their time evolution. *Mater Charact* **146**, 189–203 (2018).
59. R. Gagné, Expansive agents, in *Science and Technology of Concrete Admixtures* (Elsevier, 2016), pp. 441–456.
60. L. N. Plummer, E. Busenberg, The solubilities of calcite, aragonite and vaterite in CO2-H2O solutions between 0 and 90°C, and an evaluation of the aqueous model for the system CaCO3-CO2-H2O. *Geochim. Cosmochim. Acta* **46**, 1011–1040 (1982).
61. M. Wu, B. Johannesson, M. Geiker, A review: Self-healing in cementitious materials and engineered cementitious composite as a self-healing material. *Construct. Build Mater.* **28**, 571–583 (2012).
62. G. Yildirim, M. Sahmaran, H. U. Ahmed, Influence of hydrated lime addition on the self-healing capability of high-volume fly ash incorporated cementitious composites. *J. Mater. Civ. Eng.* **27**, 04014187 (2015).
63. C. Edvardsen, Water permeability and autogenous healing of cracks in concrete. *ACI Mater. J.* **96**, 448–454 (1999).
64. M. Bechthold, J. C. Weaver, Materials science and architecture. *Nat. Rev. Mater.* **2**, 17082 (2017).

Acknowledgments: We would like to thank the archaeological area and the archaeological museum of Priverno, as well as the community of Priverno, particularly M. Cancellieri, N. Cassieri, and F. Di Mario for cooperation and assistance in providing access to the Privernum archaeological site. The reconstruction data shown here were collected with the expertise of Gianfranco Quaranta of Artech Lab and Roberto Scalesse of the Erresse Group, both of whom are members of Associazione per la Ricerca e l'Educazione nell'Arte, Archeologia e Architettura (AREA3). The self-healing experiments were conducted with the help of P. Tudori of the Istituto Meccanica dei Materiali (IMM). We dedicate this paper in memoriam of mastro Gilberto

Quarneti (1941-2021) for his contribution to ancient materials studies. **Funding:** Partial funding for this project was provided by the MIT Edward H Linde (1962) Presidential Fellowship program to Linda Seymour. **Author contributions:** Conceptualization: A.M. Supervision: A.M. Methodology: L.M.S., J.M., P.S., M.D.T., J.C.W., and A.M. Investigation: L.M.S., J.M., P.S., M.D.T., J.C.W., and A.M. Visualization: L.M.S., J.M., and J.C.W. Writing—original draft: L.M.S. and A.M. Writing—review and editing: L.M.S., J.M., P.S., M.T., J.C.W., and A.M. **Competing interests:** P.S. and A.M. are stakeholders in DMAT srl. A.M. and L.M.S. are inventors of patent applications related to the results presented herein, assigned to the Massachusetts Institute of Technology (published as WO 2019/204776). DMAT srl has certain rights to commercialize these patent applications. P.S. and M.D.T. are listed as inventors of the International (PCT) application entitled "Building materials" (PCT/IB2022/000353), filed 7 April 2022, and claiming priority to U.S. provisional application no. 63/171,770, entitled "Building materials" and filed 7 April 2021. The other authors declare that they have no competing interests. **Data and materials availability:** All data needed to evaluate the conclusions in the paper are present in the paper and/or the Supplementary Materials.

Submitted 27 May 2022
Accepted 28 November 2022
Published 6 January 2023
10.1126/sciadv.add1602